Advances in Aircraft and Spacecraft Science, *Vol. 11, No. 2 (2024) 177-194*
https://doi.org/10.12989/aas.2024.11.2.177

Influence of geometrical parameters of reentry capsules on flow characteristics at Mach 6

R.C. Mehta*

Department of Aeronautical Engineering, Noorul Islam Centre for Higher Education, Kumaracoil 629180, India

(Received May 28, 2024, Revised July 30, 2024, Accepted August 16, 2024)

Abstract. The objective of this paper is to compute entire flow field over Apollo-II, Aerospace Reentry Demonstrator (ARD), Orbital Experiment (OREX) with sharp shoulder and rounded shape shoulder and Space Recovery Experiment (SRE) at different flare-cone half-angle of 20° and 35°. This paper addresses numerical solutions of the compressible three-dimensional Euler equations on hexahedral meshes for a freestream Mach 6 and at an angle of incidence 5°. Furthermore, spatial discretization is accomplished by a cell centred finite volume formulation solution and advanced in time by an explicit multi-stage Runge-Kutta method. The flow field characteristics, distribution of surface pressure coefficient and Mach number on fore-body and aft-body are presented as a function of the geometrical parameters of many reentry capsules. The surface pressure variation is numerically integrated to obtain the aerodynamic drag and compared well with impact theory. The present numerical study has observed the significant dependence of the blunt body and the aft-body geometry of the vehicle and can be used to study atmospheric conditions during re-entry trajectory. The numerical analysis reveals the significant influence of capsule geometry on the flow characteristics of the mechanism of upstream and structure of the flow near the wake region and aerodynamic drag coefficient.

Keywords: aerodynamics; base flow; computational fluid dynamics; hypersonic flow; reentry capsule; shock wave; surface pressure coefficient

1. Introduction

The term capsule customarily employed to describe a variety of spacecraft viz. manned mission spacecraft, planetary probes and aero-assist flight experiments. Allen and Eggers (1958) brought the concepts of the blunt body for reentry capsule that reduces aerodynamic heating and generates high aero-braking. The trajectory of the capsule alters drastically depending on the ballistic coefficient, which is directly proportional mass of the capsule and inversely proportional to the drag coefficient, and the reference area. The trajectories are classified as lifting (skipping or diving), non-lifting (steep or shallow), terminal (gravity assist), thrusting (jet-on) reentry. Selection of geometric parameters (Otsu 2021) of space capsules is a major task for improving its volumetric efficiency, ballistic coefficient, flight performance and aerodynamic heating for safe and smooth recovery. Shape of reentry capsules (Mehta 2019a) can be classified as, head-light shape as in the case of Soyuz, a bell shape in the case of Apollo, saucer type in the case of Orbital

*Corresponding author, Ph.D., E-mail: drrakhab.mehta@gmail.com

http://www.techno-press.org/?journal=aas&subpage=7 ISSN: 2287-528X (Print), 2287-5271 (Online)

Experiment (OREX), umbrella shape in the case of Express Recovery of Space System (EXPRESS), Delft Aerospace Recovery Test (DELFT) and Space Recovery Experiment (SRE) capsules.

High speed aerodynamics of a blunt-nose body are analytically explained by Truitt (1959). They found analytically that Newtonian-plus-centrifugal theory has a singular point where the first approximation to the pressure vanishes 60^o for the sphere. Thus, for a sphere, the surface pressure vanishes at 60^o from the front stagnation point.

The Euler code (SANDIAC) has been developed by Noack and Lopez (1988) to compute flow fields for a large number of vehicle geometry. Inviscid and thin layer Navier-Stokes algorithms are employed to obtain lift, drag, and moment coefficients of Commercial Experiment Transporter (COMET) re-entry vehicle for various Mach number and angle of attack by Wood *et al.* (1996). Afilipoae, *et al.* (2015) developed a three-dimensional compressible unstructured Euler solver for high speed flows over various vehicles. Computational fluid dynamics (CFD) method is used by Liever *et al.* (2003) to compile aerodynamic data sheets for the Beagle-2 capsule. Barnhardt *et al.* (2010) presented CFD analysis of CUBRC base flow. Flow fields over various blunt-nose body capsules are numerically evaluated by Viviani and Pezzella (2010a). Orion Crew Module (OCM) aerodynamic testing has been carried out by Murphy *et al.* (2011). A conceptual design method has been employed for shape optimization for a space reentry module by Zhemiz *et al.* (2011). Kazemba *et al.* (2012) carried out a comprehensive investigation of blunt body characteristics using experimental, analytical and computational methods. Neville and Candler (2015) have performed CFD based axisymmetric aero-shell shape optimization in hypersonic entry conditions. Aerodynamic data of many reentry modules is compiled by Weiland (2014). Flow field and aerodynamic characteristics of the Crew Module (CM) at Mach 4 are numerically obtained using FLUENT commercial code by Desikan *et al.* (2015). Aerothermodynamic characteristics of various space reentry vehicles are presented by Viviani and Pezzella (2015b). Raju (2015) carried out axisymmetric CFD simulation using FLUENT software for evaluating aerodynamic drag of the Phoenix capsule. Hypersonic flow past a spherically blunted nose-cone body has been analysed to obtain normal density ratio, shock standoff distance, and drag coefficient by Hornung *et al.* (2019). Hu *et al.* (2017) numerically simulated flow field characteristics of hypersonic flow over a blunt body reentry module. Conceptual shape optimization of various entry vehicles have been studied by Dirkx *et al.* (2017). Multi-objective hypersonic entry aero-shell shape optimization has been carried out by Theisinger (2009). Hypersonic blunt-body shape optimization for reducing drag has been carried out by Seager and Agarwal (2017). Aerodynamic drag is a function of bluntness ratio that has been numerically obtained for several axisymmetric bodies at zero angle of incidence by Narayan *et al.* (2019). Influence of the Mars atmospheric model on aerodynamics of an entry capsule has been carried out using DSMC code by Zuppardi (2019). Giorgio *et al.* (2019) presented an aerothermodynamics design optimization framework for hypersonic vehicles. Rashid *et al.* (2023) considered a CFD analysis of a reentry Apollo model AS-202 capsule entering the atmosphere of Earth. Scattela (2022) presented aerodynamic analysis of the ExoMars capsule during Mach 5 Mars atmospheric descent. Mwaene *et al.* (2024) carried out aerodynamic design of Mars ascent vehicles. Numerical simulations of Orion Crew Module (OCM) have been carried out by Stremel *et al.* (2011) for various trajectory conditions. Lappas *et al.* (2024) presented the design of miniature reentry vehicle for Mesosphere exploration.

Cassanto (1971), Nieden and Olivier (2007) and McLaughlin *et al.* (2011) used orbit determination that relies on the measurement of back and fore-body pressure at a point as the capsule surface in aerodynamic shadow. Rose and Brauckmann (2011) conducted aerodynamic

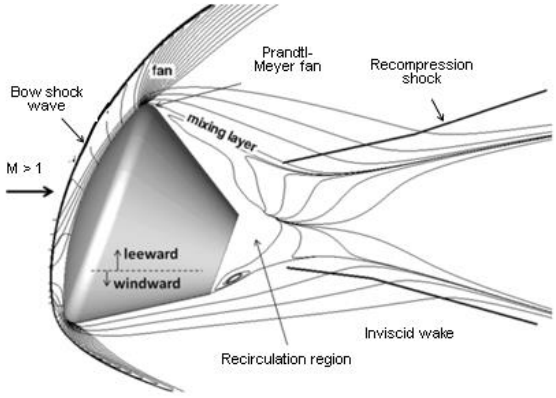

Fig. 1 Schematic sketch of inviscid flow field over a reentry capsule

and aero-acoustic wind-tunnel testing of the Orion Crew Module. Aerodynamic forces are measured by Laurence *et al.* (2012) on a scale model capsule in a high enthalpy shock tunnel. It is important to mention here that a string is required to mount the model in a wind tunnel testing. The presence of sting attachment disturbs the structure of shear layer confluence at the downstream of base region of the module.

A schematic sketch of an inviscid flow field over a reentry capsule at an angle of attack is shown in Fig. 1. A bow shock wave is formed ahead of the forebody. The bow shock wave becomes weak due to pressure relief provided by the axisymmetric shape of the capsule. The flow turns around the shoulder of the capsule as depicted in Fig. 1. A Prandtl-Meyer expansion fan appears on the shoulder of the capsule and the pressure decreases rapidly. A low-pressure zone appears immediately downstream of the base which is characterized by a low-speed recirculating flow region. A complex inviscid flow field structure includes a recompression shock. Hypersonic reentry capsule wake flow field at angle of incidence became asymmetric (Lin *et al.* 2006). Base flow consists of corner expansion, recompression zone and re-circulation flow. Shock wave is formed at this point, called the recompression shock. Beyond the neck is the far field, which extends for many body diameters downstream as the momentum deficit created by the passing capsule is slowly recovered. Capsule experienced being pulled and pushed due to formation of high pressure on the front region and low pressure in the base region, respectively.

The present paper numerically simulates flow field characteristics over various capsules at Mach 6 and angle of attack of 5^{o}. Computed flow field and surface pressure distributions over Apollo-II, Aerospace Reentry Demonstrator (ARD), Orbital EXperiment (OREX) with sharp shoulder and rounded shape shoulder and Space Recovery Experiment (SRE) at different flare-cone half angle of 20^{o} and 35^{o} capsules are numerically integrated to obtain drag. Numerical results are compared well with the Newton impact theory. The objective of this work is to investigate the influence of geometrical parameters on characterization of the mechanism of upstream and structure of the flow near the wake region.

2. Numerical analysis

2.1 Governing equations

Three-dimensional compressible Euler equations accurately describe wave drag, shock location, shock pressure rise. Euler equations admit a vortical solution when a flow passes by a blunt body, a repeating pattern of swirling vortices is generated. The governing fluid dynamic equations can be written as

$$\frac{\partial \boldsymbol{U}}{\partial t}+\frac{\partial \boldsymbol{E}}{\partial x}+\frac{\partial \boldsymbol{F}}{\partial y}+\frac{\partial \boldsymbol{G}}{\partial z}=0 \tag{1}$$

where the conservative vector $\boldsymbol{U}$, and the convective inviscid flux vector $\boldsymbol{E}$, $\boldsymbol{F}$ and $\boldsymbol{G}$ are written as vectors

$$\boldsymbol{U}=\begin{bmatrix}\rho\\ \rho u\\ \rho v\\ \rho w\\ \rho e\end{bmatrix}, \boldsymbol{E}=\begin{bmatrix}\rho u\\ \rho u^2+p\\ \rho uv\\ \rho uw\\ (\rho e+p)u\end{bmatrix}, \boldsymbol{F}=\begin{bmatrix}\rho v\\ \rho vu\\ \rho v^2+p\\ \rho vw\\ (\rho e+p)v\end{bmatrix}, \boldsymbol{G}=\begin{bmatrix}\rho w\\ \rho uw\\ \rho vw\\ \rho w^2+p\\ (\rho e+p)w\end{bmatrix} \tag{2}$$

Temperature is related to the perfect gas equation of state. The ratio of the specific heats was assumed constant value and its value taken as 1.4. where the determinant of the Jacobian matrix transformed from the Cartesian coordinate system to the cylinder coordinate system Mwaene *et al.* (2024). At M=6, there is insufficient energy to cause dissociation of the gas, therefore a perfect gas model is employed, with specific heats ratio γ=1.4, in numerical simulations.

2.2 Numerical algorithm

The numerical algorithm uses a finite volume discretization technique. The computational domain is divided into several hexahedral cells. The conservative variables $\boldsymbol{U}$ within each cell are calculated from their average values at the cell centre. The convective flux vectors $\boldsymbol{E}$, $\boldsymbol{F}$ and $\boldsymbol{G}$ are computed on each side of the cell. The spatial and temporal terms are decoded using the method of lines. The finite volume code constructed in this way reduces to a central difference scheme and it is second order accurate in space and time, provided the mesh is smooth enough. The flow solver and boundary conditions are described (Mehta *et al.* 2023b) and also validated results with experimental data of Subramanian *et al.* (1996).

2.3 Geometrical details of reentry capsules

The dimensional details of the Apollo-II capsule shown in Fig. 2(a) are of axisymmetric design. The forebody has a truncated sphere with a rounded shoulder. The Apollo-II (11900 kg), the apex of the conical after body, was removed to form a flat base section for docking purposes. The Apollo-II capsule has a spherical blunt body diameter of D=3.95 m, spherical nose radius of R_N=4.74 m and a shoulder radius of R_C=0.1973 m. the back shell has an inclination angle α_B=33º relative to the capsule's axis of symmetry as depicted in Fig. 2(a). The overall length L of the capsule is 2.686 m.

The ARD (2753 kg) (ESA's Atmospheric Reentry Demonstrator) capsule is an axisymmetric design with a spherical blunt nose diameter D=2.80 m, and spherical cap radius, R_N=3.36 m and a shoulder radius, R_C=0.014 m, an overall length L=2.04 m. The ARD shape is sketched in Fig. 2(b) and globally resembles a 70% scaled Apollo capsule. The relief angle α_B of the main after body is 33º.

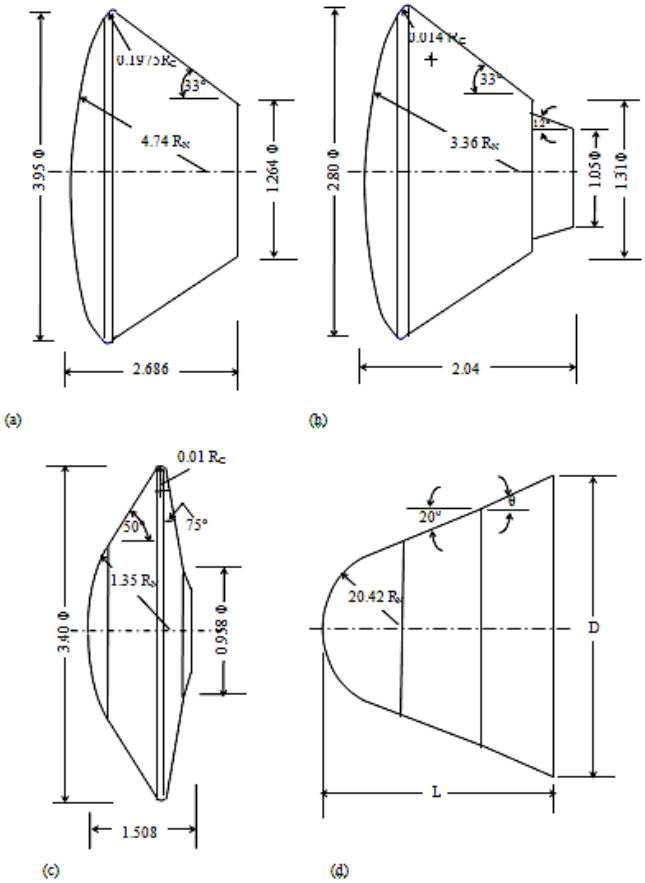

Fig. 2 Dimensions of (a) Apollo-II, (b) ARD, (c) OREX and (d) SRE capsules

Table 1 Geometrical variables of SRE capsules

SRE	D, m	S, m^2	L, m	θ
M1	0.07391	0.00429	0.05721	20^o
M3	0.08229	0.00538	0.05719	35^o

The OREX (760 kg) (Orbital Reentry EXperiment) geometry is shown in Fig. 2(c) with rounded shoulders. The forebody shape is composed of a spherical nose, cone and a circular shoulder. The OREX geometry is displayed in Fig. 2(c). The forebody shape consists of spherical cap radius R_N=1.33 m, a half-cone angle α_N=50^o, D=3.40 m, L=1.508 m and R_C=0.01 m. the OREX geometry incorporates a rear cover with a small backward step at the junction between back cover and heat shield. The aft body is having a α_B=15^o, half-cone angle relative to the plane of symmetry. Blunting in the form of a flat surface with a rounded shoulder and referred to as OREX-C.

The SRE (550 kg) (Space Recovery Experiment) model is an axisymmetric design. The SRE module consists of a 20° blunt-nosed cone of nose radius R_N=0.02042 m followed by a flare-section with a flare-cone angle θ that can take values of 20° and 35°. The dimensions of the SRE

Table 2 Number of grid points and cells in computational domain

Capsule	Number of grid points	Number of cells	Stretching factor
Apollo-II	114×30×17, 125×30×17	58140, 63750	1.2
ARD	104×30×17, 110×30×17, 152×30×17	53040, 56100, 77520	1.2
OREX	108×30×17, 140×30×17	55080, 71400,	1.2
OREC-C	120×30×17,	61200	1.2
SRE, θ=20^o	104×30×17, 140×30×17,	53040, 71400	1.5
SRE, θ=35^o	202×30×17, 212×30×17, 222×30×17,	103020, 108120, 113220	1.5

capsule considered in the numerical analysis are shown in Fig. 2(d) and tabulated in Table 1.

2.4 Computational grid

Proper selection of the computational grid is crucial in numerical simulations for capturing the complex flow features such as bow shock, expansion fan, recirculation zones, recompression shock and wake trail region as shown in Fig. 1. The grids are well aligned to anticipate these flow features. The computational cells are generated employing finite element methods in conjunction (Mehta 2011c). Mono-block, non-overlapping structured grids are generated and then rotated in the azimuthal direction in an orderly manner. The computational domain is having a single-block by joining four connecting computational regions. The grids in the computational domain were composed of hexahedral meshes. The mesh is stretched from the wall to calculate surface pressure. The outer boundary of the computational domain is kept as 1.5-2.5 times the base diameter *D*. In the downstream direction, the computational boundary is about 6-8 times *D*. The number of grid points and cells in axial, circumferential, and normal to the capsule is shown in Table 2. This grid arrangement is found to yield a relative difference of about ±5% in the computation of fore body aerodynamic drag coefficient. Fig. 3(a) to 3(e) show symmetry planes of the mesh over the Apollo-II, ARD, OREX-C with rounded shoulders and OREX with sharp shoulders, and SRE 20^o and 35^o capsules, respectively. Several grid arrangements are considered as tabulated in Table 2 to verify the grid's independence. The numerical results are presented in the next section.

3. Results and discussion

3.1 Flow characteristics

We are presenting in Fig. 4 Mach contour over Apollo-II, ARD (Fig. 4 (a), (b)) schematic sketch resembling as a bell shape Fig. 4(c), OREX with rounded shoulder, OREX with sharp shoulder (Fig. 4 (d), (e)) schematic sketch similar as a saucer shape Fig. 4(f), and SRE θ=20^o and θ=35^o (Fig. 4 (g), (h)) schematic sketch of look as an umbrella capsule Fig. 4(i), respectively. The Mach contour captured all the essential flow features over the reentry capsules as shown in Fig. 1. A bow shock wave stands in front of all the capsules but their shape depends on the geometry of the fore-body of the capsules. The bow shock wave follows the fore-body and; the fore-body is entirely subsonic up to the shoulder of the Apollo, the ARD and the OREX capsules. In the case of the spherically blunted cone-fare capsule, the sonic line is located at the junction of the sphere

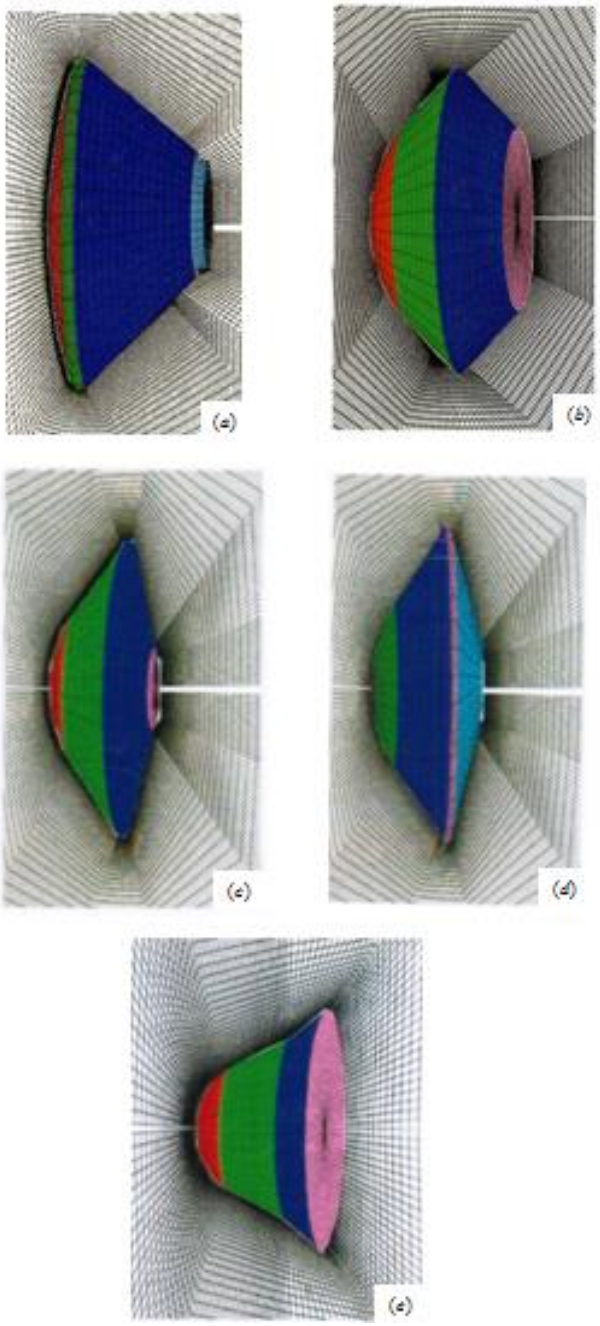

Fig. 3 Three-dimensional computational grid over (a) Apollo-II, (b) ARD, (c) OREX-C with rounded shoulder, (d) OREX with sharp shoulder, (e) SRE capsule

cone as seen in Mach contour of the SRE. We found a Prandtl-Meyer expansion fan over the shoulder of the capsules. However, the expansion fan is gradually turning over the rounded shoulder as compared with the sharp corner of the OREX capsule as depicted in Fig. 4(d). The

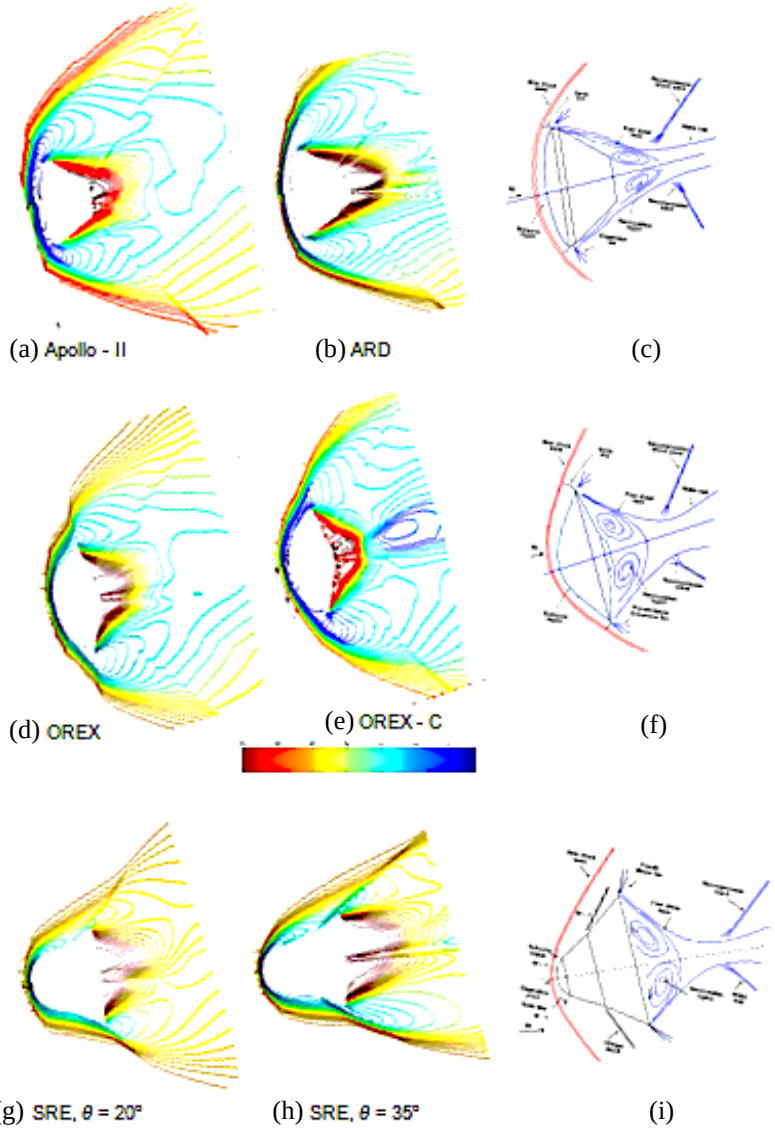

Fig. 4 Mach contour over Apollo-II, ARD, schematic sketch of a bell shape capsule (c), OREX with bevel shoulder, OREX with sharp shoulder schematic sketch of a saucer shape capsule (f), SRE θ=20° and θ=30° schematic sketch of an umbrella capsule (i)

flow field over the capsule becomes complicated due to the presence of the shoulder and the base shell of the capsules as depicted in figure.

The Mach contours in the plane of symmetry over the SRE capsules at cone-flare angles θ=20°, and 35° at α=5°. It can be observed from the Mach contours that the flow field in the wake region depends on the cone-flare angle. The flow field becomes asymmetric due to angle of attack. The flow significantly altered in the windward and the leeward side of the SRE. The flow characteristics depend on the flare half cone angle. Mach contour reveals that the size of the recirculation zone is sensitive to the capsule shape. Mach contours have noted the significant

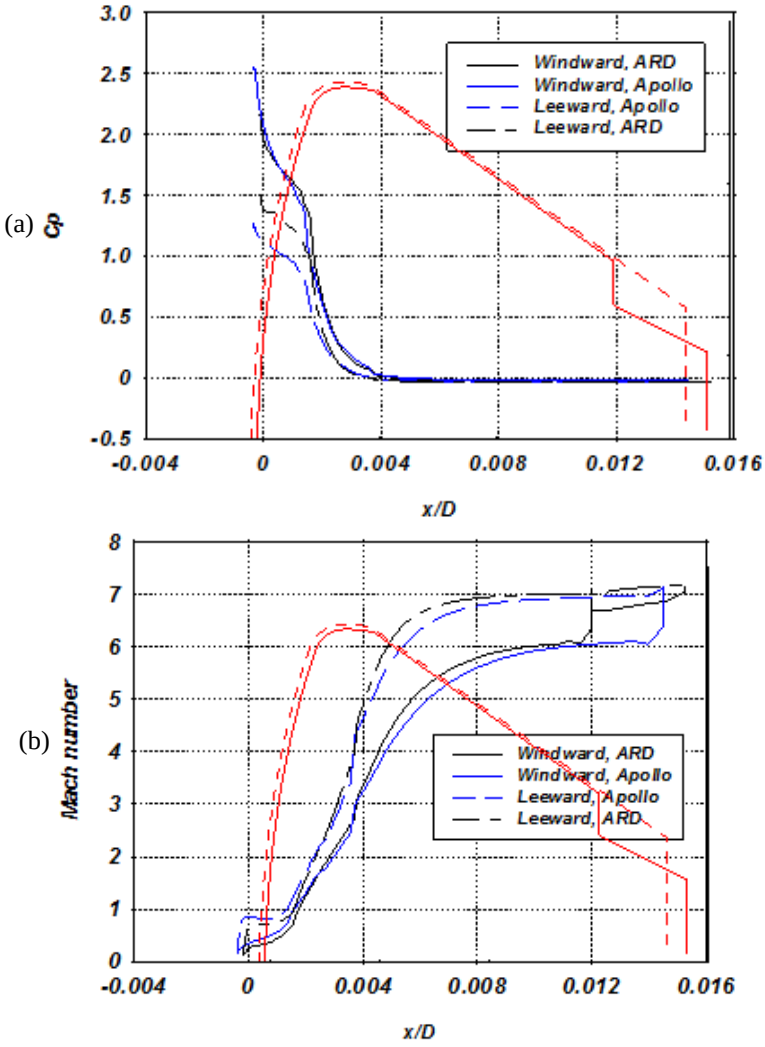

Fig. 5 Variation of wall (a) pressure coefficient (b) Mach number over fore-body of Apollo-II and ARD

dependence of the blunt body dynamics on the aft-body geometry of the vehicle. Volumetric requirements need that an entry vehicle have an appreciable length of aft-body. This means the larger volume inside the capsule should be better from the viewpoint of the payload.

3.2 Surface pressure and mach number variations

Figs. 5 to 10 show surface pressure coefficient and surface Mach number over the fore body and base of the capsules at Mach 6 and angle of attack 5°. The x/D=0 represents the stagnation point, where x is the distance measured along the surface from the stagnation point.

Fig. 5 (a) and (b) shows the variation of wall pressure coefficient Cp and wall Mach number over the Apollo-II and the ARD capsules, respectively. For the sake of clarity we have also drawn the outer geometry of the capsules in the figures. It can be easily noticed the influence of

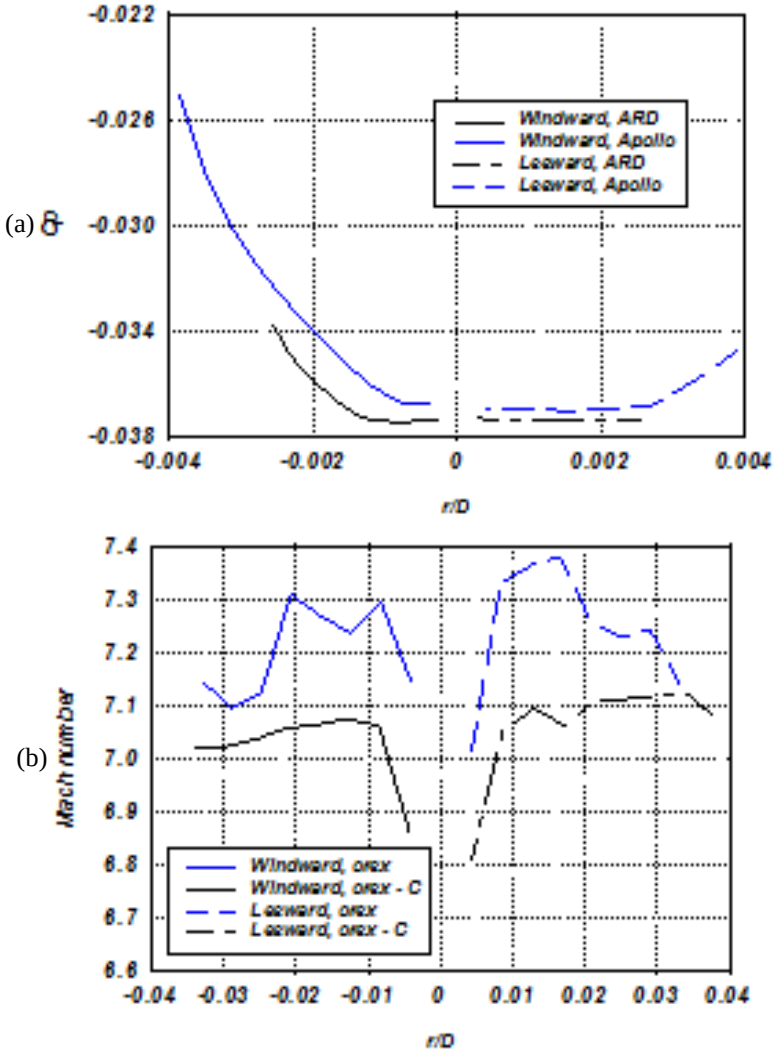

Fig. 6 Variation of wall (a) pressure coefficient (b) Mach number over base of the Apollo-II and the ARD capsule

geometrical parameters on the *Cp* and Mach distributions. The ARD capsule is 70% of the Apollo. The aft-body of the ARD is having additional attachment that effects appear in the *Cp* and Mach distributions.

Fig. 6 (a) and (b) depicts the variation of base pressure coefficient and the Mach number over the Apollo-II and the ARD capsules, respectively. A significant difference in base pressure and Mach number is noticed between the Apollo-II and the ARD capsules. A low pressure is formed immediately downstream of the base which is characterized by a low-speed flow region.

Fig. 7 (a) and (b) shows variation of surface pressure and Mach over the fore body of the OREX-C with the rounded shoulder and the OREX with a sharp corner, respectively. The pressure and Mach distributions over the fore body depend on the geometry of the shoulder of the OREX capsule. It is also worth comparing with the fore-body pressure and Mach distribution between the

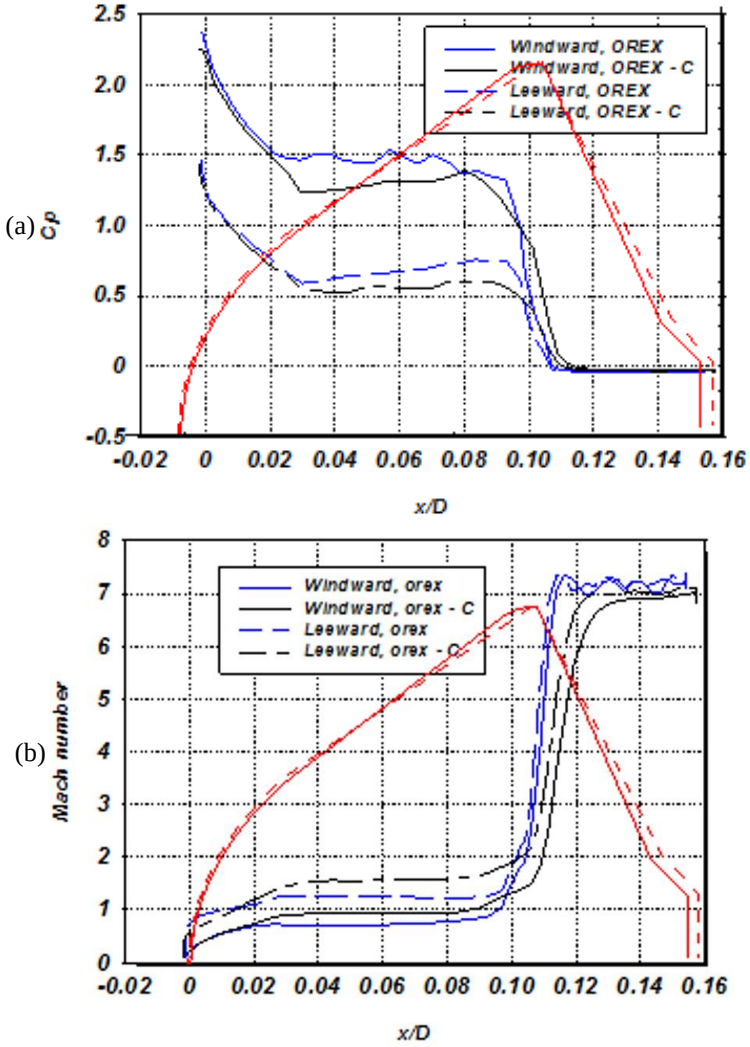

Fig. 7 Variation of wall (a) pressure coefficient (b) Mach number over fore-body of OREX with bevel shoulder and with sharp shoulder

Apollo-II and the OREX. The pressure variation over the fore body varies gradually due to spherical shape whereas in the case of the OREX change in variations can be noticed on the junction of sphere and cone junction of the OREX.

Fig. 8 (a) and (b) depicts the variation of base pressure coefficient and the Mach number over the OREX-C and the OREX. We also observed the influence of the shoulder on the pressure and Mach distribution on the base of the OREX-C and the OREX. The pressure coefficient is decreased due to rounded shoulders but Mach number profile shows increase of Mach number on the base of the capsule. A low pressure is formed immediately downstream of the base which is characterized by a low-speed flow region.

Fig. 9 (a) and (b) shows the variations of surface pressure coefficient *Cp* and wall Mach number over the SRE for flare-cone angle θ=20º and 35º. It shows significant differences in the

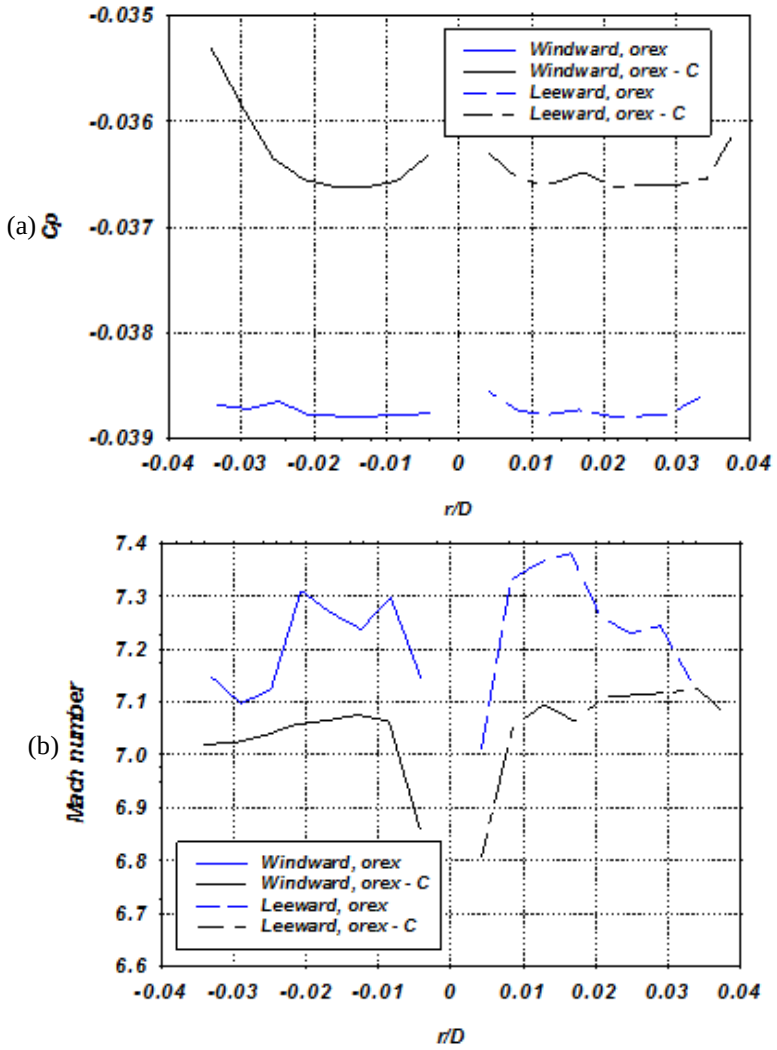

Fig. 8 Variation of wall (*a*) pressure coefficient (*b*) Mach number over base of OREX with bevel shoulder and with sharp shoulder

pressure coefficient and Mach number variations on the fore body of the SRE. Fig. 9 also displays geometry of the SRE with *Cp* to determine influence of flare-cone angle. The pressure coefficient gradually falls on the sphere-cone region and remains constant over the cone section of the SRE model due to supersonic flow. The surface pressure distribution decreases in the cone-flare section. It can be seen from Fig. 9 the influence of flare-cone angle θ. There is waviness in the *Cp* variation over the cone-flare of 35° half cone angle due to unsteadiness. To analyse unsteady flow requires solving viscous equations. The purpose of the present numerical simulation is to analyse the influence of geometrical parameters of the capsule for preliminary design of the reentry capsules using inviscid flow solver. The inviscid analysis will also provide a basic flow field due to change of fore-body, shoulder radius and cone-flare angle. A sudden drop in *Cp* is observed on the shoulder of the module followed by a negative *Cp* variation in the base region. A low pressure is

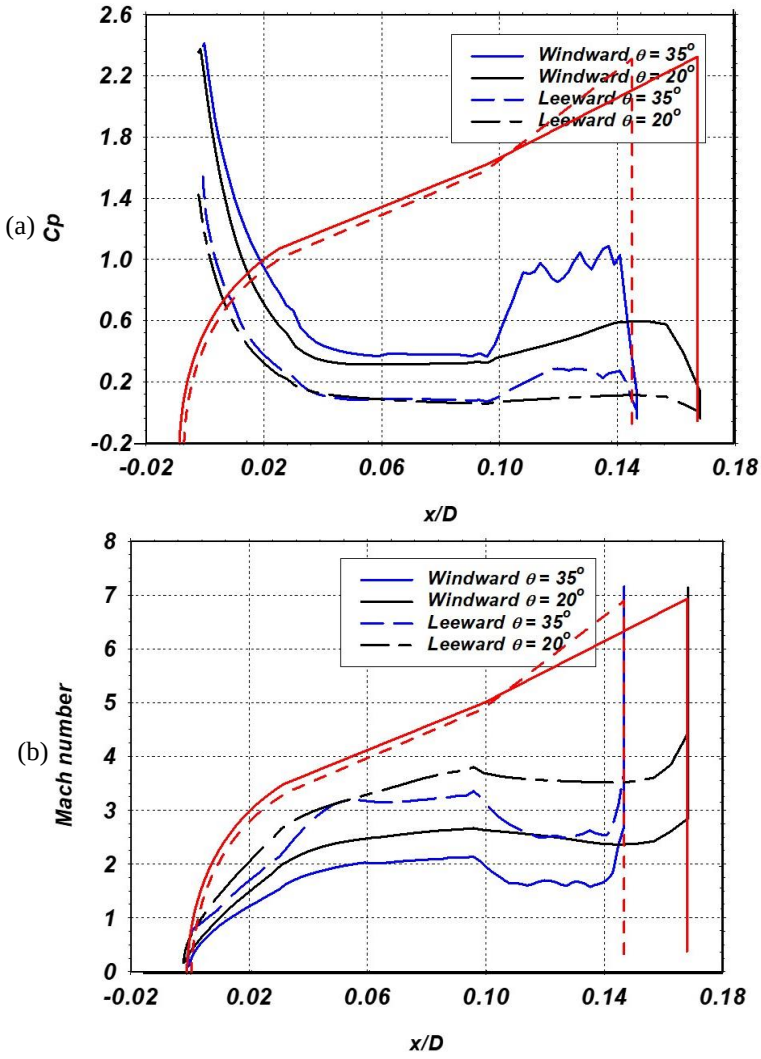

Fig. 9 Variation of wall (a) pressure coefficient (b) Mach number over fore-body of SRE θ=20° and 35°

formed immediately downstream of the base which is characterized by a low-speed flow region. In the base region, *Cp* is decreasing with increasing flare-cone angle. Rapid expansion around the forebody corners produces high Mach numbers in the outer inviscid region of the wake.

Fig. 10 (a) and (b) shows the radial base pressure coefficient and Mach number distributions on the base of the SRE capsule. On the base of the SRE model, the pressure coefficient is decreasing with increasing flare half cone angles. Constant local pressure coefficient is found in the base region. It reveals the formation of a low-pressure region near the base attributed to rapid expansion. It is observed that the Mach number reaches up to about 7 on the corner point of the SRE. The variations of windward and leeward side Mach number over the base of the SRE at α=5° is also displayed. It is found that the Mach number reaches up to about 5.5 in the base region of the SRE.

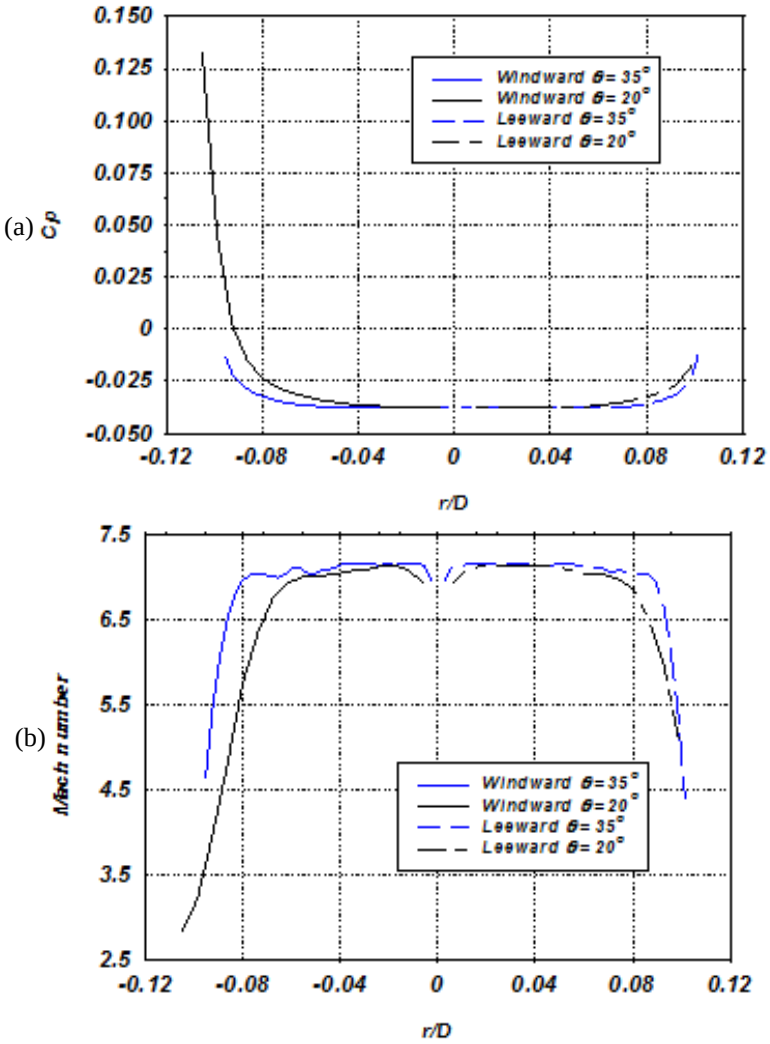

Fig. 10 Variation of wall (a) pressure coefficient (b) Mach number over base of SRE θ=20^o and 35^o

It is important to mention that it is difficult to measure base pressure in the wind tunnel due to the presence of sting attachment. More importantly, the base pressure at the leeward plane is higher than the leeward base wall pressure. These results indicate that there is significant upstream influence from the base flow upon the base flow fields.

3.3 Fore-body aerodynamic drag

Wave drag is calculated by integrating the surface pressure variation on the fore-body of the capsules that is excluding the base drag. Newtonian model (Bertin 1994) is employed to compute the aerodynamic drag which is based on the assumption that the freestream maintains its speed and direction unchanged until it strikes the surface exposed to the flow. The impact theory does not specify the pressure that does not visualize the flow, that is the surface on which gas dynamics

Table 3 Fore-body drag of Apollo-II, ARD, OREX with rounded corner and sharp corner

Capsule	$C_{D,F}$	
	CFD	Newtonian
Apollo-II	1.50	1.54
ARD	1.44	1.48
OREX-C	1.40	1.44
OREX	1.12	1.15

Table 4 Fore-body drag of SRE capsules

Capsule	θ=20º	θ=35º
	$C_{D,F}$	
CFD	0.38	0.48
Newtonian	0.37	0.47

would predict Prandtl-Meyer flow. When the flow is curved in the direction of the freestream the difference in pressure from the shock wave the body surface equals the centrifugal force due to curvature of the flow. Lee (1955) proposed a modified Newtonian theory which consists in scaling down so as to be at a stagnation point, where the correct value is known. The Newtonian flow assumption was used to calculate $C_{D,F}$ for Apollo-II, ARD, OREX with rounded shoulders and sharp corners is shown in Table 3. Fore-body aerodynamic drag of SRE capsule for θ=20º and 35º. is shown in Table 4. A comparison between CFD and the Newtonian flow is also given in Tables 3 and 4, and exhibits agreement between them. Aerodynamic drag on the fore-body also reveals the influence of the geometrical parameters of the capsules.

4. Conclusions

Flow fields over a Apollo-II, ARD, OREX with rounded corner and sharp shoulder, SRE with semi flare-cone angle of 20º and 35º reentry capsules are numerically computed by solving the three-dimensional compressible inviscid equations for Mach 6 at angle of attack 5º. The flow field over the capsule depends on external geometry of the capsule and freestream conditions. The size of the recirculation zone is sensitive to the capsule shape. The flow features downstream of the bow shock wave are more defined for the sharp cornered body relative to those for the forebody with the rounded shoulder. Surface pressure coefficient and surface Mach number distributions over the capsules show the influence of the geometrical parameters. A good agreement is found between calculated aerodynamic coefficients with the Newtonian impact theory.

References

Afilipoae, T.P. and Stoia-Djeska, M. (2015), "Development of a three-dimensional unstructured euler solver for high-speed flows", *Incas Bulletin*, **7**(4), 3-18. https://doi.org/10.13111/2066-8201.2015.7.4.1.

Allen, H.J. and Eggers, J. (1958), "A study of the motion and aerodynamic heating of ballistic missiles entering the Earth's atmosphere at high supersonic speeds", Ames Aeronautical Laboratory, Moffett Field, California, NACA TR-1381.

Barnhardt, M. and Candler, G.M. (2010), "CFD analysis of CUBRC base flow experiments", *48th AIAA Aerospace Sciences Meeting Including the New Horizons Forum and Aerospace Exposition*, 1250. https://doi.org/AIAA 10.2514/6.2010-1250.

Bertin, J.J. (1994), *Hypersonic Aerothermodynamics*, AIAA Education Series, American Institute of Aeronautics and Astronautics, Washington DC, USA.

Cassanto, J.M. (1971), "Full scale flight test base pressure results for a blunt planetary reentry probe configuration", *J. Spacecraft Rocket.*, **8**(9), 996-998. https://doi.org/10.2514/3.30338.

Desikan, S.L.N., Patil, M.N. and Subramanian, S. (2015), "Understanding of flow features over a typical crew module at Mach 4", *Aeronaut. J.*, **119**, 727-746. https://doi.org/10.1017/S0001924000010794.

Dirkx, D. and Mooji, E. (2017), *Conceptual Shape Optimization of Entry Vehicles*, Springer Cham, Germany.

Giorgio, S.D., Quagliarella, D., Pezzella, G. and Pirozzoli, S. (2019), "An aerothermodynamics design optimization framework for hypersonic vehicles", *Aerosp. Sci. Technol.*, **84**, 339-347. https://doi.org/10.1016/j.ast.2018.09.042.

Hornung, H., Martinez Schramm, J. and Hannemann, K. (2019), "Hypersonic flow over spherically blunted cone modules for atmospheric entry. Part 1. The sharp cone and the sphere", *J. Fluid Mech.*, **871**, 1097-1116. https://doi.org/10.1017/jfm.2019.342.

Hu, Y., Huang, H. and Zhang, Z. (2017), "Numerical simulation of a hypersonic flow past a blunt body", *Int. J. Numer. Meth. Heat Fluid Flow*, **27**(6), 1351-1364. https://doi.org/10.1108/HFF-05-2016-0187.

Kazemba, C.D., Braun, R.D., Clark, I.G. and Schoenenberger, M. (2012), "Survey of blunt body dynamic stability in supersonic flow", *AIAA Atmospheric Flight Mechanics Conference*, 4509. https://doi.org/10.2514/6.2012-4509.

Lappas, V., Klothakis, A., Nikolos, I. and Theofilis, V. (2024), "On the design of miniature re-entry vehicles for Mesosphere exploration, Part I: Theoretical consideration", *AIAA SCITECH 2024 Forum*, 1160. https://doi.org/10.2514/6.2024-1160.

Laurence, S.J., Schramm, J.M. and Hannemann, K. (2012), "Force and moment measurements on a free-flying capsule model in a high-enthalpy shock tunnel", *28th Aerodynamic Measurement Technology, Ground Testing, and Flight Testing Conference including the Aerospace T&E Days Forum*, 2861. https://doi.org/10.2514/6.2012-2861.

Lee, L. (1955), *Hypersonic Flow*, Institute Aeronautical Science, Preprint No. 554.

Liever, P.A., Habchi, S.D., Burnell, S.I. and Lingard, J.S. (2003), "Computational fluid dynamics prediction of the Beagle 2 aerodynamic data base", *J. Spacecraft Rocket.*, **40**(5), 632-638. https://doi.org/10.2514/2.691.

Lin, T.C., Sproul, L.K., Kim, M., Olmos, M. and Feiz, H. (2006), "Hypersonic reentry vehicle wake flow fields at angle of attack", *44th AIAA Aerospace Sciences Meeting and Exhibit*, 582. https://doi.org/10.2514/6.2006-582.

McLaughlin, C.AS., Mance, S. and Lechtenberg, T. (2011), "Drag coefficient estimation in orbit determination", *J. Astonaut. Sci*., **58**(3). 513-530. http://doi.org/10.1007/BF03321183.

Mehta, R.C. (2017c), "Multi-block structured grid generation for computational fluid dynamics", *Scholar J. Eng. Technol.*, **5**(8), 387-219. https://doi.org/10.21276/sjet.

Mehta, R.C. (2019a), "Numerical simulation of base pressure and drag of space re-entry capsules at high speed, hypersonic vehicles-past, present and future developments", *Hypersonic Vehicles-Past, Present and Future Developments*, UK. https://doi.org/10.5772/intechopen.83651.

Mehta, R.C. and Rathakrishan, T. (2023b), "Computation of aerodynamic coefficients of a re-entry capsule at Mach 6", *Adv. Aircraft Spacecraft Sci.*, **10**(5) 457-471. https://doi.org/10.12989/aas.2023.10.5.457.

Murphy, K.J., Bibb, K.L., Brauckmann, G.J., Rhode, M.N., Owens, B., Chan, D.T., Walker, E.L., Bell, J.H. and Wilson, T.M. (2011), "Orion crew module aerodynamic testing", *29th AIAA Applied Aerodynamics Conference*, 3502. https://doi.org/10.2514/6.2011-3502.

Mwaene, E. and Banda, L.O.L. (2024), "Aerodynamic design and performance analysis of Mars ascent vehicles", Qeios ID: VJ9NXB. https://doi.org/10.32388/VJ9NXB.

Narayan, A., Narayanan, S., Kumar, R., Kumar, C.S. and Jagadeesh, G. (2019), "Hypersonic flow past a

spherically blunted nose cone: A computational study", *Progr. Comput. Fluid Dyn.*, **20**(2), 105-123. https://doi.org/10.1504/PCFD.2019.10026157.

Neville, A.G. and Candler, G.V. (2015), "Computational fluid dynamics based axisymmetric aero-shell shape optimization in hypersonic entry conditions", *J. Spacecraft Rocket.*, **52**(1), 76-88. https://doi.org/10.2514/1.A32678.

Nieden, P.Z. and Olivier, H. (2007), "Determination of atmospheric densities from reentry flight data", *J. Spacecraft Rocket.*, **44**(2) 332-337. https://doi.org/10.2514/1.19338.

Noack, R.W. and Lopez, A.R. (1988), "Inviscid flow field analysis of complex vehicles: Vol. I Description of numerical methods", Report SAND-0776/1, Sandia National Laboratory.

Otsu, H. (2021), "Aerodynamic characteristics of re-entry capsules with hyperbolic contours", *Aerosp.*, **8**, 287. https://doi.org/10.3390/aerospace8100287.

Ottens, H.B.A. (2001), "Preliminary computational investigation on aerodynamic phenomena DELFT aerospace reentry test vehicle", *Proceedings of the 4th European Symposium on Aerothermodynamics for Allocations*, ESA Capua, Italy.

Raju, M. (2015), "CFD analysis of mars phoenix capsules at Mach Number 10", *J. Aeronaut. Aerosp. Eng.*, **4**(01), 4-7. https://doi.org/10.4172/2168-9792.100014.

Rashid, F.L., Hussein, V., Habeeb, L.J., Hussein, A.K., Hamida, M., Ali, B. and Younis, O. (2023), "Numerical thermal analysis of re-entry Apollo model AS-202", *J. Eng. Sci. Technol.*, **18**(1), 693-705.

Rose, J.C. and Brauckmann, G.J. (2011), "Aerodynamic and aero-acoustic wind-tunnel testing of the Orion Spacecraft", *29th AIAA Applied Aerodynamics Conference*, 3160. https://doi.org/10.2514/6.2011-3160.

Scattela, G. (2022), "Aerodynamical analysis of ExoMars capsule during Mach 5 Mars atmospheric descent", Master of Science in Aerospace Engineering, Università degli Studi di Padova, Italy.

Seager, C. and Agarwal, R.K. (2017), "Hypersonic blunt-body shape optimization for reducing drag and heat transfer", *J. Thermophys. Heat Transf.*, **31**(1), 48-55. https://doi.org/10.2514/1.T4650.

Stremel, P.K., McMullen, M.S. and Garcia, J.A. (2011), "Computational aerodynamic simulations of the Orion command module", *29th AIAA Applied Aerodynamics Conference*, 3503. https://doi.org/10.2514/6.2011-3503.

Subramanian, S., Kurup, M.K.A., Kalimuthu, R. and Raveendran, P.G. (1996), "An experimental investigation of hypersonic aerodynamic characteristics of re-entry bi-conic configurations at Mach 6", Vikram Sarabhai Space Centre, Trivandrum, India.

Theisinger, J.E. and Braun, R.D. (2009), "Multi-objective hypersonic entry aeroshell shape optimization", *J. Spacecraft Rocket*, **46**(5), 957-966. https://doi.org/10.2514/1.41136.

Truitt, R.W. (1959), *Hypersonic Aerodynamics*, Ronald Press, New York, USA.

Viviani, A. and Pezzella, G. (2010a), "Computational flowfield analysis over a blunt-body re-entry vehicle", *J. Spacecraft Rocket.*, **47**(2), 258-270. https://doi.org/10.2514/1.40876.

Viviani, A. and Pezzella, G. (2015b), *Aerodynamic and Aerothermodynamic Analysis of Space Mission Vehicles*, Springer International Publishing A.G., Switzerland.

Walpot, L.M.G., Wright, M.J., Noeding, P. and Schrijer, F. (2012), "Base flow investigation of the Apollo AS-202 command module", *Progr. Aerosp. Sci.*, **48-49**, 57-74. https://doi.org/10.1016/j.paerosci.2011.06.006.

Weiland, C. (2014), *Aerodynamic Data of Space Vehicles*, Springer-Verlag, Berlin Heidelberg, Germany.

Wood, W.A., Gnoffo, P.A. and Rault, D.F.G. (1996), "Aerothermodynamic analysis of Commercial Experiment Transporter (COMET) reentry capsule", *34th Aerospace Sciences Meeting and Exhibit*, 316. https://doi.org/10.2514/6.1996-316.

Zhenmiz, Z., Yunliancy, D., Yi, L. and Tieliang, Z. (2011), "Shape optimization design method for the conceptual design of reentry vehicles", *Acta Astonautica Sincia*, **32**(11), 1971-1979.

Zuppardi, G. (2019), "Influence of the Mars atmosphere model on aerodynamics of an entry capsule", *Adv. Aircraft Spacecraft Sci.*, **6**(3) 239-256. https://doi.org/10.12989/aas.2019.6.3.239.

Nomenclature

C_D	aerodynamic drag coefficient
Cp	pressure coefficient
D	diameter of capsule
$\boldsymbol{E}$, $\boldsymbol{F}$, $\boldsymbol{G}$	convective flux vectors
L	length of the capsule
M	Mach number
p	pressure
q_∞	dynamic pressure
R_C	shoulder radius
R_N	blunt nose radius
S	reference base surface area
$\boldsymbol{U}$	conservative variable
u, v, w	velocities in the x, y, z directions, respectively
x, y, z	Cartesian coordinate
α	angle of attack in pitch plane, *AoA*
γ	ratio of specific heats
ϕ	circumferential
θ	cone half-angle of the flare
ρ	density

Subscripts

B	base
F	front